

Received February 12, 2021, accepted March 15, 2021, date of publication March 22, 2021, date of current version March 30, 2021.

Digital Object Identifier 10.1109/ACCESS.2021.3067800

A Class-E-Based Resonant AC-DC Converter With Inherent PFC Capability

HUSSEIN MAHDI¹, (Graduate Student Member, IEEE),
AHMED M. AMMAR², (Member, IEEE), YASSER NOUR², (Senior Member, IEEE),
AND MICHAEL A. E. ANDERSEN², (Member, IEEE)

¹Department of Electrical Engineering, UiT Norges Arktiske Universitet, 8514 Narvik, Norway

²Department of Electrical Engineering, Technical University of Denmark, 2800 Kongens Lyngby, Denmark

Corresponding author: Ahmed M. Ammar (amma@elektro.dtu.dk)

This work was supported by the European Union's Horizon 2020 Research and Innovation Programme under Grant 731466.

ABSTRACT This paper investigates the use of the class-E inverter for power factor correction (PFC) applications. Analytical and state-space models are derived showing the class-E inverter's capability of achieving inherent PFC operation with a constant duty cycle. The inherent PFC operation limits the controller responsibility to the regulation of the output voltage, which is key for resonant converters with challenging control. A converter incorporating a diode bridge, a class-E inverter, and a class-D rectifier is presented for the PFC stage in single-phase offline converters. A prototype is designed to validate the analysis and presented design method. The prototype operates with zero-voltage switching (ZVS) across the load range and achieves up to 211 W of output power at an efficiency of 88 %, with an inherent power factor of 0.99 and a total harmonic distortion (THD) of 8.8 %. Frequency modulation is used to achieve lower output power down to 25 W, with a power factor of 0.95, THD of 28 %, and an efficiency of 88 %.

INDEX TERMS AC-DC power conversion, class-E inverter, power factor correction, resonant power conversion, zero-voltage switching.

I. INTRODUCTION

Large-scale deployment of switch-mode power supplies to the utility introduces line current harmonics. The injected current harmonics result in voltage distortion and reduce the reliability of the grid [1], [2]. As a result, several international standards expressly limit the magnitudes of input current harmonics and set a limit for the minimum power factor. Thus, a power factor correction (PFC) converter needs to be employed in offline converters for different applications to comply with these standards.

The typical solution for offline converters is a two-stage structure that is illustrated in Fig. 1. A front-end stage ac-dc PFC converter rectifies the ac line voltage to a relatively smooth dc voltage while regulating the input current to follow the ac line voltage. A following dc-link capacitor filters the double-the-line frequency component. Finally, a dc-dc converter provides the current and voltage levels that apply to the load. This work's focus is on the PFC front-end stage of the offline converter.

The associate editor coordinating the review of this manuscript and approving it for publication was Tariq Masood¹.

Conventionally, pulse width modulation (PWM) converters are employed for the PFC stage, including boost [3]–[6], buck [7]–[9], buck-boost [10]–[12], SEPIC [13], [14], Cuk [15], and flyback [16] topologies. They offer high power quality and efficiency [17]. However, their hard-switching nature results in high switching losses, which sets an upper limit for the switching frequency and, in turn, the power density. In addition, their sharp switching current and voltage waveforms have high-frequency harmonic components, complicating electromagnetic interference (EMI) filters design.

Resonant converters operation is based on soft switching, which results in substantially lower switching losses and EMI noise at higher switching frequencies [18], [19]. The soft-switching nature has been previously studied in class-E inverter [20] and class-D inverter [21]. As a result, resonant converters have been investigated for use in many applications, one of which is offline converters, where prior art reported their use in the ac-dc stage [22]–[25], dc-dc stage [26]–[29], or both stages [30]–[32].

This paper investigates the feasibility of employing the class-E inverter for the PFC stage in single-phase offline

FOCUS OF THIS WORK

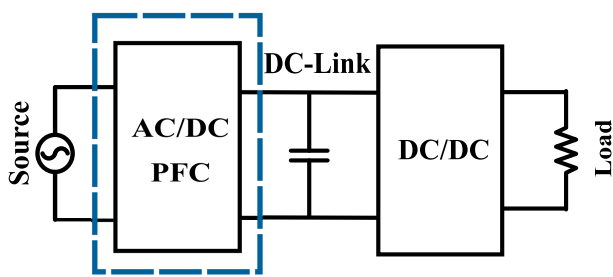


FIGURE 1. Offline converter structure.

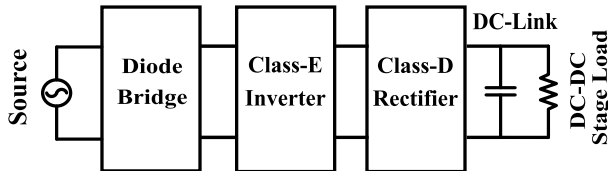


FIGURE 2. The architecture of the proposed converter.

converters [33]. Mathematical models are derived for the circuit showing inherent PFC capability with a constant duty-cycle operation. A converter comprising an input bridge, a class-E inverter, and a class-D rectifier is presented. Fig. 2 shows the proposed converter block diagram. The converter operation is based on zero-voltage switching (ZVS) and achieves PFC inherently. The inherent PFC operation limits the controller responsibility to the regulation of the output voltage, which is key for resonant converters with challenging control. At the same time, the soft-switching operation enables the design of PFC converters with high switching frequencies and power densities.

This paper is organized as follows: Section II describes the principle of operation of the presented converter. Mathematical models based on analytical and state-space approaches are covered in Section III. Section IV presents the design procedure. Prototype implementation and experimental verification results are illustrated in Section V. Finally, conclusion is provided in Section VI.

II. PRINCIPLE OF OPERATION

The schematic of the presented converter is shown in Fig. 3, which comprises a front-end diode bridge rectifier $D_1 - D_4$, a class-E inverter, and a class-D current-driven rectifier. The diode bridge rectifies the ac input voltage. A capacitor C_{in} is connected in parallel with the bridge to suppress the EMI and absorb the reverse current from the inverter. A class-E ZVS inverter drives the resonant tank with a current $i_r(t)$, where the shape of the waveform depends on the loaded quality factor of the tank Q_L and the duty-cycle D . A class-D rectifier converts the high-frequency current into a dc output voltage V_o , where the voltage stress across the rectifier diodes equals the output voltage.

Considering that the switching frequency f_s is much higher than the line frequency f_l , the input voltage to the inverter $v_{rec}(t)$ is assumed constant across the switching

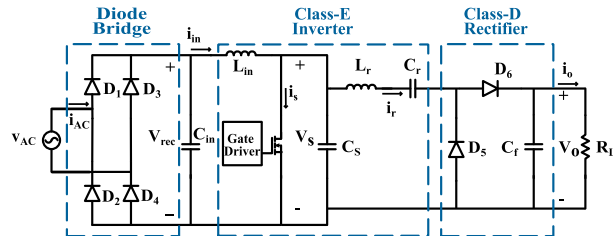


FIGURE 3. Class-E converter for PFC applications.

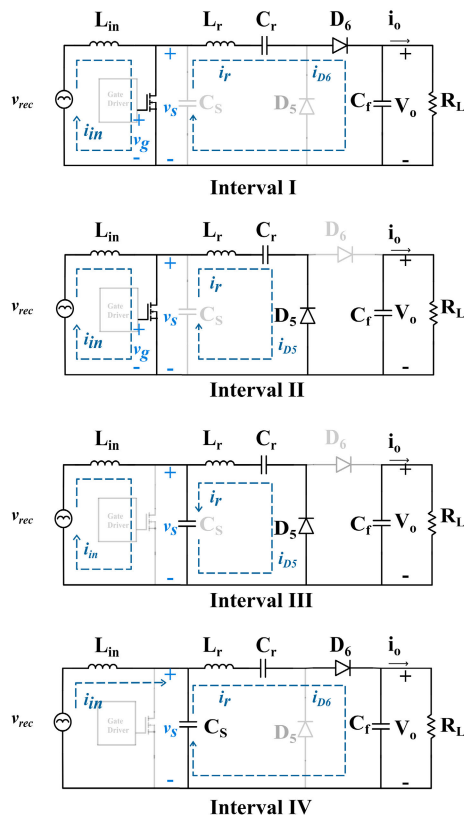


FIGURE 4. Simplified circuit diagram for a half-line cycle operation.

cycle. With a high-enough quality factor for the resonant tank, the first-harmonic approximation (FHA) approach for modeling resonant converters is valid, and the resonant current is a sinewave with the form

$$i_r(\theta_s) = I_r \sin(\theta_s + \phi) \tag{1}$$

where I_r is the current amplitude, $\theta_s = \omega_s t$ is the current angle across the switching cycle, and ϕ is the phase shift with the switching node voltage.

The switching cycle is divided into four intervals, as shown in Fig. 4, with the corresponding voltage and current waveforms illustrated in Fig. 5, including the voltage across the switch gate $v_g(t)$, the drain-source voltage of the switch, i.e. switching node voltage $v_s(t)$, the inverter input current $i_{in}(t)$, the resonant current $i_r(t)$, and the diodes currents $i_{D5}(t)$ and $i_{D6}(t)$.

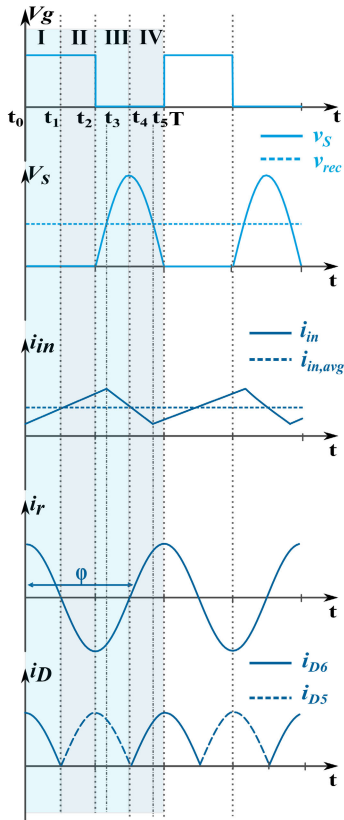


FIGURE 5. Voltage and current waveforms across two switching cycles.

In interval I ($t_0 - t_1$), the switch is on and the rectified voltage $v_{rec}(t)$ is higher than $v_s(t)$, thus the input current $i_{in}(t)$ increases linearly, charging the input inductor L_{in} . The resonant current is positive and flows in D_6 , while D_5 is in reverse bias. Accordingly, the current flowing through the switch is the difference between $i_{in}(t)$ and $i_r(t)$.

In interval II ($t_1 - t_2$), the switch is still on, and the input current $i_{in}(t)$ keeps charging the input inductor L_{in} , while the resonant current reverses its direction and flows in D_5 with D_6 in reverse bias.

In interval III ($t_2 - t_4$), the switch is turned off and the capacitor C_s starts charging with the input current. Thus, $v_s(t)$ begins to increase, yet it is still less than the $v_{rec}(t)$. As a result, $i_{in}(t)$ keeps increasing until it reaches its maximum at t_3 when $v_{rec}(t)$ equals $v_s(t)$. Afterwards, the input inductor L_{in} starts discharging in the capacitor C_s , resulting in increasing of the voltage stress across the switch to its maximum value by the end of this interval.

In interval IV ($t_4 - T$), the switch is still turned off, the resonant current reverses its direction, turning D_5 off and D_6 on. The capacitor C_s starts discharging, and the switch voltage reduces until $v_{rec}(t)$ equals $v_s(t)$ at t_5 , with the inductor L_{in} discharging as $v_{rec}(t) < v_s(t)$. From t_5 to the end of the interval, the inductor L_{in} is charging, and the capacitor C_s continues discharging until full depletion. By the end of this interval, the switch is turned on by the gate driver, and a new cycle begins.

If the switching frequency is higher than the resonant frequency f_o of the series-resonant tank ($L_r - C_r$), the tank and rectifier represent an inductive load and ZVS can be achieved. That is shown in Fig. 5 where the switch turns on at zero voltage, with a negative current in the resonant tank. By modulating the switching frequency f_s with respect to the resonant frequency f_o , the converter gain changes and accordingly the output power is modulated. The choice of the duty cycle affects ZVS operation as well as the stress on the switch. Theoretically, the switch voltage stress in a class-E inverter reaches about 3.6 times the input voltage with 50 % duty cycle [34]. However, in practice, this stress could reach more than four times the input voltage due to the nonlinearity of the switch node capacitance C_s [35], [36]. Accordingly, this topology is more suited for low-input-voltage applications.

III. MATHEMATICAL MODELLING

In this section, the mathematical models for the class-E inverter are investigated with respect to the input impedance. The conventional analytical and state-space approaches are considered. In the former approach, the design procedure derives the equations from the waveforms, while the latter is based on the basic circuit equations from Ohm’s and Kirchhoff’s laws. The principle of operation of the class-E rectifier as an input current shaping stage explained in [31], [32] is adopted in this work.

A. ANALYTICAL APPROACH

The analysis of the proposed topology is carried out across the switching cycle and using the approach given in [34], which assumes an ideal semiconductor switch and a high-enough input inductance such that the dc component of the input current I_{in} is only considered. From the principle of operation given in Section II and the V_s waveform in Fig. 5, the capacitor C_s current can be written as follows

$$i_{C_s}(\theta_s) = \begin{cases} 0, & 0 < \theta_s \leq 2\pi D \\ I_{in} - I_r \sin(\theta_s + \phi), & 2\pi D < \theta_s \leq 2\pi \end{cases} \quad (2)$$

The voltage across the switch is then calculated

$$\begin{aligned} v_s(\theta_s) &= \frac{1}{\omega_s C_s} \int_0^{\theta_s} i_{C_s}(\theta) d\theta \\ &= \begin{cases} 0, & 0 < \theta_s \leq 2\pi D \\ \frac{1}{\omega_s C_s} \{ I_{in}(\theta_s - 2\pi D) \\ + I_r [\cos(\theta_s + \phi) - \cos(2\pi D + \phi)] \}, & 2\pi D < \theta_s \leq 2\pi \end{cases} \quad (3) \end{aligned}$$

where θ is the variable of integration. Under optimal operation conditions, where ZVS is achieved, the voltage across the switch equals zero by the end of the switching period. Substituting $\theta_s = 2\pi$ in (3) and equating to zero, the following

expression for the resonant current amplitude is derived.

$$I_r = I_{in} \frac{2\pi(1-D)}{\cos(2\pi D + \phi) - \cos(\phi)} \quad (4)$$

Considering zero-derivative voltage switching (ZdVS, $dv_s(2\pi)/d\phi = 0$) is also achieved, taking the derivative for (3) with $\theta_s = 2\pi$ and equating to zero, the following expressions for the phase shift ϕ is derived.

$$\tan(\phi) = \frac{\cos(2\pi D) - 1}{2\pi(1-D) + \sin(2\pi D)} \quad (5)$$

It can be seen that ϕ is a function of the duty cycle D . Following, the rectified voltage can be written as follows

$$V_{rec} = \frac{1}{2\pi} \left[\int_0^{2\pi} v_{L_{in}}(\theta) d\theta + \int_0^{2\pi} v_s(\theta) d\theta \right] \quad (6)$$

As the average voltage across the input inductor is zero, eliminating the first term and substituting (3) in (6) then evaluating the integration gives

$$V_{rec} = \frac{I_{in}}{\omega_s C_s} \left\{ \frac{(1-D)[\pi(1-D)\cos(\pi D) + \sin(\pi D)]}{\tan(\pi D + \phi)\sin(\pi D)} \right\} \quad (7)$$

Dividing (7) by I_{in} gives the following expression for the input resistance.

$$R_{in} = \frac{1}{\omega_s C_s} \left\{ \frac{(1-D)[\pi(1-D)\cos(\pi D) + \sin(\pi D)]}{\tan(\pi D + \phi)\sin(\pi D)} \right\} \quad (8)$$

Since (8) is a function of the duty cycle D and phase shift ϕ , which is itself a function of duty cycle as shown by (5), then operating with a constant duty cycle results in a constant input resistance that is independent of line changes. As a result, the converter is seen as a resistor from the input across the line cycle and power factor correction is achieved.

B. STATE-SPACE APPROACH

While the analytical approach assumes an ideal switching device and a sinusoidal resonant current to ensure the validity of the FHA approach, in the state-space approach, the design parameters are computed numerically. The state-space approach is used in prior art [37]–[39] to design class-E dc-dc converters with any loaded quality factor of the resonant tank and any size for the input inductor. Accordingly, it is considered in this section for flexibility across different designs.

By adding the switch on-resistance to the model, the switch is replaced with a resistor as follows

$$r_s = \begin{cases} r_{on}, & 0 < \theta_s \leq 2\pi D \\ r_{off}, & 2\pi D < \theta_s \leq 2\pi \end{cases} \quad (9)$$

where r_{on} and r_{off} are the equivalent resistances of the switch in on- and off-states, respectively. The circuit has four energy storage components (L_{in} , L_r , C_s and C_r), which define the dimension of the state vector. The following expressions are

obtained by applying Kirchhoff voltage and current laws.

$$\begin{cases} \omega_s L_{in} \frac{di_{in}(\theta_s)}{d\theta_s} = v_{rec}(\theta_s) - v_s(\theta_s) \\ \omega_s C_r \frac{dv_{C_r}(\theta_s)}{d\theta_s} = i_r(\theta_s) \\ \omega_s L_r \frac{di_r(\theta_s)}{d\theta_s} = v_s(\theta_s) - v_{C_r}(\theta_s) - i_r(\theta_s) R_{eff} \\ \omega_s C_s \frac{dv_s(\theta_s)}{d\theta_s} = i_{in}(\theta_s) - \frac{v_s(\theta_s)}{r_s} - i_r(\theta_s) \end{cases} \quad (10)$$

where $v_{C_r}(\theta_s)$ is the voltage across the resonant tank capacitor C_r and R_{eff} is the class-D rectifier effective resistance. By normalizing the impedance in (10) with the effective resistances, it can be rearranged and rewritten in the following matrix form

$$\dot{x} = A \cdot x + B \cdot u \quad (11a)$$

$$A = \begin{bmatrix} \frac{1}{\omega_s C_s r_s} & 0 & \frac{1}{\omega_s R_{eff} C_s} & \frac{-1}{\omega_s R_{eff} C_s} \\ 0 & 0 & 0 & \frac{1}{\omega_s R_{eff} C_r} \\ \frac{-R_{eff}}{\omega_s L_{in}} & 0 & 0 & 0 \\ \frac{Q_L}{Q_L} & 0 & \frac{-1}{Q_L} & \frac{-1}{Q_L} \end{bmatrix} \quad (11b)$$

$$B = \begin{bmatrix} 0 \\ 0 \\ \frac{R_{eff}}{\omega_s L_{in}} \\ 0 \end{bmatrix} \quad (11c)$$

$$x = \begin{bmatrix} v_s(\theta_s) \\ v_{C_r}(\theta_s) \\ i_{in}(\theta_s) \\ i_r(\theta_s) \end{bmatrix} \quad (11d)$$

$$Q_L = \frac{\omega_s \cdot L_r}{R_{eff}} \quad (11e)$$

where x is the state vector, A is the system matrix, B is the control matrix, and u is the input vector. From (11), the number of parameters is nine, i.e. ω_s , D , Q_L , L_{in} , L_r , C_r , C_s , R_{eff} , $r_s \in \mathbb{R}^9$, and the solution of the equation is

$$x(\theta_s) = x_n(\theta_s) + x_f(\theta_s) \quad (12)$$

where $x_n(\theta_s)$ is the natural response of the system and $x_f(\theta_s)$ is the forced response. These two terms can be calculated as follows [40].

$$x_n(\theta_s) = e^{A\theta_s} \cdot x(0^-) \quad (13a)$$

$$x_f(\theta_s) = A^{-1} \cdot (e^{A\theta_s} - I) \cdot B \cdot u \quad (13b)$$

where $e^{A\theta_s}$ is the exponential matrix, $x(0^-)$ is the initial condition vector, and I is the identity matrix, while the currents are normalized with the input current and the voltages are normalized with the input voltage. Since the waveforms are continuous and periodic, the initial conditions can be found by applying the continuity condition of the waveforms such that

$$x_{on}(0^-) = x_{off}(\theta)|_{\theta=2\pi(1-D)} \quad (14a)$$

TABLE 1. Design specifications.

Parameters	Specifications
RMS Input Voltage (V)	120
Line Frequency (Hz)	60
Output Power (W)	300
Output Voltage (V)	200
Switching Frequency (kHz)	90

$$x_{off}(0^-) = x_{on}(\theta)|_{\theta=2\pi D} \quad (14b)$$

Substituting (12)–(14) in (11) gives

$$\begin{bmatrix} x_{on}(2\pi) \\ x_{off}(2\pi) \end{bmatrix} = \begin{bmatrix} -e^{2\pi DA_{on}} & I \\ I & -e^{2\pi(1-D)A_{off}} \end{bmatrix}^{-1} \cdot \begin{bmatrix} A_{on}^{-1}(e^{2\pi DA_{on}} - I) \\ A_{off}^{-1}(e^{2\pi(1-D)A_{off}} - I) \end{bmatrix} \cdot B \quad (15)$$

where A_{on} and A_{off} are the system matrices in (11) when r_s is equal to r_{on} and r_{off} , respectively. Under optimal operation conditions, where ZVS and ZdVS are achieved, (15) can be re-evaluated and solved numerically using the Matlab *fsolve* solver. However, there are nine parameters and two optimum operation conditions. Therefore, ω_s , D , Q_L , L_{in} , L_r , R_{eff} , $r_s \in \mathbb{R}^7$ are chosen as the design parameters, while C_r and C_s are solved as unknown parameters.

Since (11) is in the form of a first-order differential equation, the solution with oscillating input can also be written as

$$x(\theta_l) = M \cos(\theta_l) + N \sin(\theta_l) = G \sin(\theta_l - \alpha) \quad (16a)$$

$$G = \sqrt{M^2 + N^2} = \frac{B}{\sqrt{2}} \quad (16b)$$

$$\alpha = \tan^{-1}\left(\frac{N}{M}\right) = \frac{\omega_l}{A} \quad (16c)$$

where M and N are solution parameters that are found from the initial conditions, $\theta_l = \omega_l t$ is the input current angle across the line cycle, G is the gain vector, and α is the phase shift matrix. Equation (16a) mathematically shows that the response of the system, $i_{in}(\theta_l)$ which is the main interest, to the oscillating input voltage has the same frequency of the input and phase-shifted by α . From (16c), it can be proven that the input current is in phase with the input voltage (i.e. $\alpha \approx 0$), and hence the converter emulates a resistor.

IV. CONVERTER DESIGN

This section describes the design procedure of the presented converter. Table 1 summarizes the converter design specifications. The converter is designed to operate from US mains input voltage for a rated output power of 300 W and an output voltage of 200 V. A 90-kHz switching frequency is chosen for this design which is intended to prove the analysis and inherent PFC capability. Fig. 6 shows the normalized switches voltage and current stresses with respect to the input voltage and current. A duty cycle of 40 % is chosen for minimal stress on the switch.

In the analytical approach, the design procedure based on the FHA approach and given in [34] is followed in this paper.

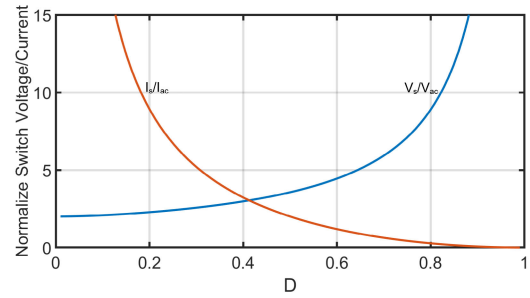


FIGURE 6. Normalized switch stresses vs. duty cycle.

To ensure the validity of the FHA approach, a high-quality factor of seven is chosen for this design. The procedure begins with the calculation of the class-D rectifier effective input resistance.

$$R_{eff} = \frac{2R_L}{\pi^2} = \frac{V_o^2}{\pi^2 \cdot P_o} \quad (17)$$

where R_L is the load resistance, V_o is the output voltage, and P_o is the output power. The phase angle of the resonant current can be written as

$$\phi = \pi + \arctan\left(\frac{\cos(2\pi D) - 1}{2\pi(1-D) + \sin(2\pi D)}\right) \quad (18)$$

The capacitor C_s is calculated from (19), as shown at the bottom of the next page. The switching frequency is chosen to be higher than the resonant frequency such that the net impedance of the tank is inductive. The inductor L_r can be divided into two series inductances, such that L_{r1} resonates with the capacitor C_r at the switching frequency, while L_{r2} is responsible for the phase lagging shown in (18) and can be calculated from (20), as shown at the bottom of the next page. Then, the resonant capacitor can be found as follows

$$C_r = \frac{1}{\omega_s^2 L_{r1}} = \frac{1}{\omega_s^2 (L_r - L_{r2})} = \frac{1}{\omega_s (Q_L \cdot R_{eff} - \omega_s L_{r2})} \quad (21)$$

The input inductance L_{in} should be large enough to ensure a small ripple current through the choke (10 % of dc current), and calculated as follows.

$$L_{in} \geq \frac{7R_{eff}}{f_s} \quad (22)$$

Regarding the output capacitor C_f , it needs to be large enough to filter the double-the-line frequency in single-phase PFC applications, and is calculated from the following expression, with η being the efficiency, and ω_l being the angular line frequency [32].

$$C_f \geq \frac{\eta P_o}{0.04 V_o^2 \omega_l} \quad (23)$$

The state-space approach is carried out numerically in MATLAB. Table 2 lists the calculated values of the components from both models. It can be observed that the values obtained from both models are highly correlated.

TABLE 2. Calculated component values.

Component	Analytical Model	State-Space Model	Difference (%)
L_{in} (μH)	205.84	205.84	0
L_r (μH)	350.59	350.59	0
C_s (nF)	15.19	14.74	3.01
C_r (nF)	11.74	12.50	6.27

TABLE 3. Bill of materials.

Component	Value	Type
$D_1 - D_4$	GBU10A	Bridge Rectifier
C_{in} (μF)	1	SMD Film Capacitor
L_{in} (mH)	1.3	3C97 ETD49/25/16
Q_1	C3M0075120D	1200-V SiC MOSFET
C_s (nF)	15	SMD Ceramic Capacitor
L_r (μH)	342.9	3C97 ETD59/31/22
C_r (nF)	2×5.6	SMD Ceramic Capacitor
$D_5 - D_6$	C3D10065A	SiC Schottky Diode
C_f (μF)	470	250-V Electrolytic Capacitor

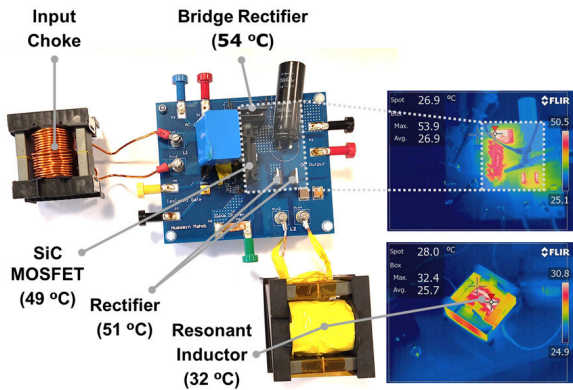


FIGURE 7. Prototype picture and thermal performance at full load.

V. PROTOTYPE IMPLEMENTATION AND EXPERIMENTAL VERIFICATION

This section covers the implementation of a prototype built based on the analysis and design procedure. Experimental results are then presented and discussed.

A. IMPLEMENTATION

The prototype of the proposed topology is assembled on a two-layer PCB. Fig. 7 shows a picture of the prototype, and Table 3 lists the bill of materials based on the parameters obtained from the design procedure given in Section IV. Compared with silicon devices, wide-bandgap devices have reduced reverse-recovery charge and better figures of merit [41]–[43]. Considering the high voltage stress across the switch, a silicon carbide (SiC) device is more suited for this application than a gallium nitride (GaN) device, as the breakdown voltage limit for commercially available GaN devices is 650 V. Cascade GaN device structures offer higher breakdown voltages up to 900 V, yet that comes with higher on-resistance than otherwise offered by SiC devices, which is a key parameter for soft-switching topologies. The C3M0075120D device by Cree/Wolfspeed is chosen and is driven using a single-channel isolated gate driver (UCC5350SBD by Texas Instruments). From (22),

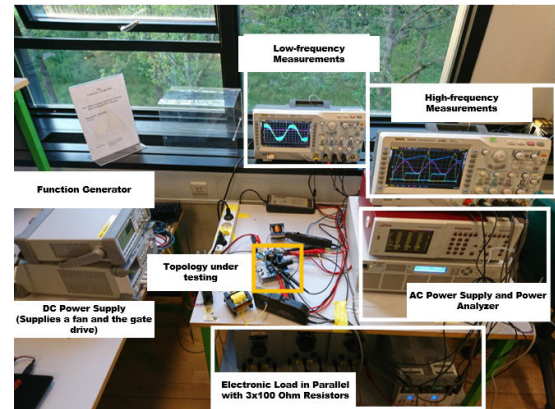


FIGURE 8. Prototype under testing.

a minimum value for the input choke of 205 μH is needed to guarantee a small ripple on the input current and ensure the validity of the analytical approach equations, where a larger value of 1.3 mH is chosen to help reduce EMI and core loss, and it does not affect the converter operation.

B. EXPERIMENTAL RESULTS

Fig. 8 shows the testing lab setup. The converter is tested from US-mains input voltage, delivering up to 211 W of power at 89.5 kHz and 55 % duty cycle, where thermal considerations limited the delivery for the specified output power.

Fig. 9 shows the line-frequency waveforms at 211 W load. The input and output voltages are measured using high-voltage differential probes (LeCroy ADP305 and Testec SI 9001), and the current is displayed using a clamp-on current probe (Siemens 7KA1412-8AA). The figure shows the input current to be proportional to the input voltage, with a minor phase difference, achieving a power factor of 0.99 inherently. The dashed waveform is the input current filtered by the moving-average function in MATLAB and shown for clarity.

$$C_s = \frac{\cos(\pi D + \phi)[(1 - D)\pi \cos(\pi D) + \sin(\pi D)] \cdot 2 \sin(\pi D) \sin(\pi D + \phi)}{\pi^2(1 - D)\omega_s R_{eff}} \quad (19)$$

$$L_{r2} = \frac{R_{eff}}{\omega_s} \cdot \frac{2(1 - D)^2\pi^2 - 1 + 2 \cos(\phi) \cos(2\pi D + \phi) - \cos(2(\pi D + \phi))[\cos(2\pi D) - \pi(1 - D) \sin(2\pi D)]}{4 \sin(\pi D) \sin(\pi D + \phi) \cos(\pi D + \phi)[(1 - D)\pi \cos(\pi D) + \sin(\pi D)]} \quad (20)$$

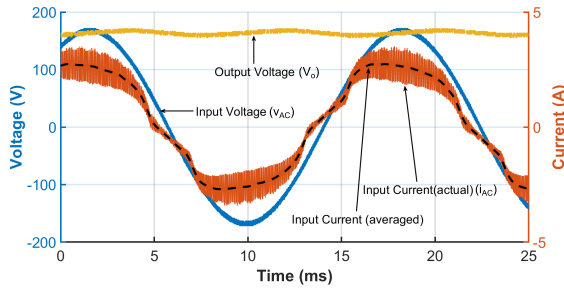


FIGURE 9. Experimental line-frequency waveforms of the proposed converter at 211 W.

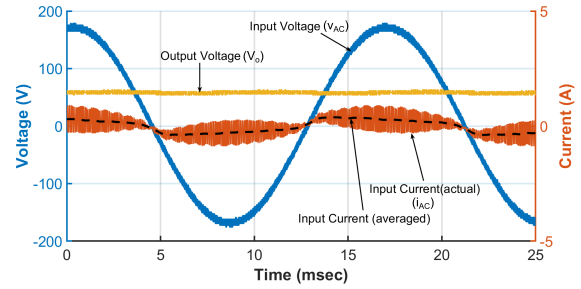


FIGURE 11. Experimental line-frequency waveforms of the proposed converter at 25 W.

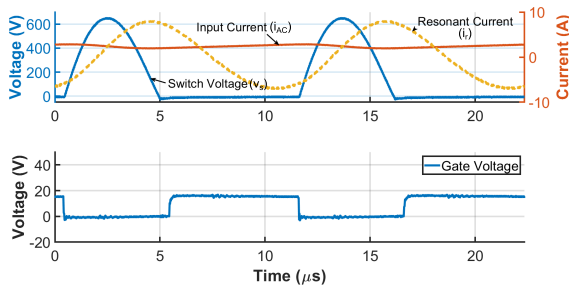


FIGURE 10. Experimental switching-frequency waveforms of the proposed converter at 211 W.

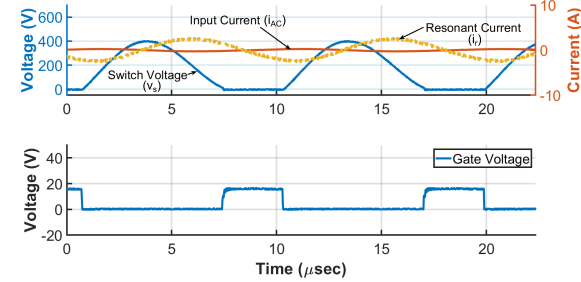


FIGURE 12. Experimental switching-frequency waveforms of the proposed converter at 25 W.

Fig. 10 shows the switching-frequency waveforms at 211 W. The resonant current has a sinusoidal waveform, which goes in accordance with the analysis and design procedure based on the FHA approach, and it is about 15 A peak-to-peak. While the input current in the inductor L_{in} is mainly a dc component with 0.4 A peak-to-peak ripple. The figure illustrates the inductive mode of operation, where the resonant current lags the switch node voltage and the switch voltage returns to zero before the switch is turned on, achieving ZVS.

A short interval of reverse conduction of the FET is observed, where the switch-node capacitance is fully depleted before the switch turns on. However, with the reduced reverse recovery charge in SiC devices, the contribution of reverse conduction to the overall power loss is insignificant and can be eliminated with the precise adjustment of the switch driving signal duty cycle.

Fig. 11 and 12 show the line-frequency and switching-frequency waveforms at 25 W. The figures show that a high-power factor is still achieved at the light load, where the ZVS operation is maintained through the adjustment of the switch duty cycle.

Fig. 13 shows the obtained efficiency and employed switching frequency across the load range. The results show that the output power can be regulated from 211 W down to 25 W with switching frequency modulation between 89.5 kHz to 104.3 kHz, respectively. The peak obtained efficiency is 88.3 % at 90 W with 96 kHz and a duty cycle of 0.5. The small dips in the efficiency curve are attributed to the partial loss of ZVS, which is corrected by adjusting the duty cycle. For lower output power down to 0 W (e.g. dimming

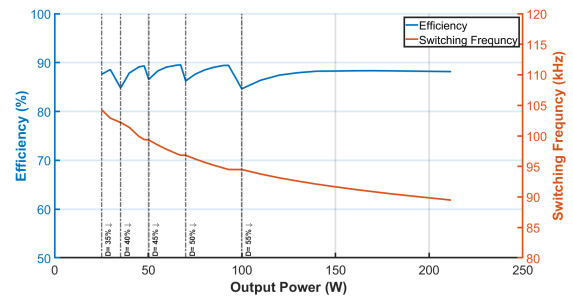


FIGURE 13. The efficiency and switching frequency of the proposed converter at different output power levels.

functionality in LED driver applications), the overall converter can be switched on/off with a low-frequency PWM signal in a burst-mode control fashion. That helps limit the maximum switching frequency of the converter and achieve high efficiency at light loads.

The power quality results are shown in Fig. 14, where a power factor of 0.99 and a total harmonic distortion (THD) of 8.8 % are achieved at full load, while the minimum power factor is 0.95 at 25 W with a THD of 28 %. The harmonic spectra of the input current at the 211 W and 25 W are illustrated in Fig. 15.

Fig. 16 shows the power loss breakdown at full load operation. The currents of the different components are obtained from experimental and simulation results, and the loss is calculated based on parameters from the devices datasheets. It can be seen that 26 % of the overall loss is incurred as conduction losses in the switch, whereas 22 % of loss is dissipated in the resonant inductor, while 30 % is lost in the rectifier diodes and 16 % in the bridge, which goes in

TABLE 4. Comparison with reported literature.

Reference	[3]	[7]	[10]	[13]	[15]	[22]	[23]	[25]	[30]	[31]	This Work
Year	2019	2015	2018	2016	2017	2020	2020	2014	2013	2009	2021
Type	PWM	PWM	PWM	PWM	PWM	Resonant	Resonant	Resonant	Resonant	Resonant	Resonant
Topology	Boost	Buck	Buck-Boost	SEPIC	Cuk	Class-D Converter	Class-D Inverter	Class-D Rectifier	Class-DE Rectifier	Class-E Rectifier	Class-E Inverter
Aux. circuit	None	Filter	None	None	Filter	None	Charge Pump	Matching Network	Matching Network	Matching Network	None
V_{in} (V _{rms})	Universal	Universal	220	120	Universal	230	230	220	220	220	120
Power (W)	1000	300	245	200	300	105	50	36.4	36	36	211
V_{out} (V)	400	80	400	400	300	450	300	342	327	343	165
PF	0.99	0.94	0.99	0.97	0.99	0.99	0.99	0.98	0.99	0.99	0.99
THD (%)	-	25.7	< 10	27.2	< 6	5.2	8.6	20	1.4	5.6	8.8
Efficiency (%)	96	97	97	96	-	94	88	94	90	86	88
Switching Frequency (kHz)	550	65	4000	50	500	2000	1000	50	84	61	90
PFC Functionality	Inherent	Controlled	Controlled	Controlled	Controlled	Controlled	Inherent	Inherent	Inherent	Inherent	Inherent
Components Count ¹	6	11	8	14	12	10	11	11	13	12	10
Switches	1	2	2	2	1	2	2	2	2	2	1
Diodes	1	2	2	5	5	2	3	2	2	1	2
Magnetic Components	1	3	1	3	3	1	1	2	2	2	2

1. Including the bridge as a single component and excluding the input filter.

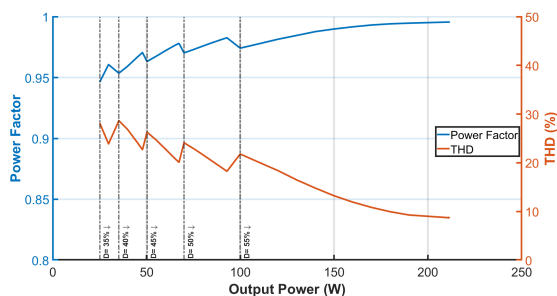


FIGURE 14. The obtained power factor and THD across load range.

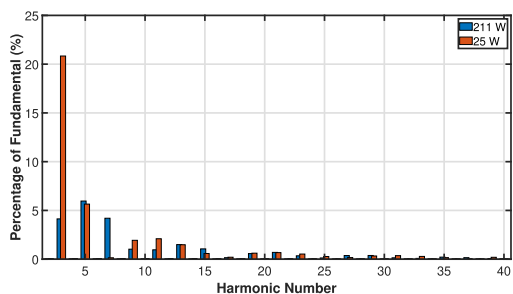


FIGURE 15. Input current harmonic spectra at 211 W and 25 W loads.

accordance with the thermal pictures in Fig. 7. By improving the resonant inductor implementation and the choice of rectifier diodes and bridge, higher efficiency can be achieved.

Table 4 compares the proposed work with a number of reported solutions for PFC applications for the low-mid

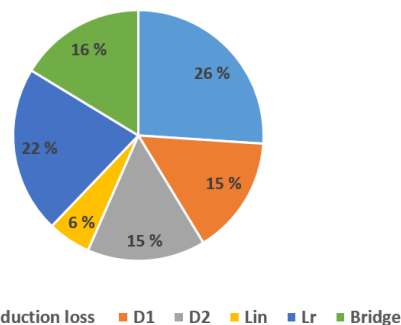


FIGURE 16. Power loss breakdown at full load.

power range. It can be observed that the obtained power factor and THD figures fall within the ranges reported by prior art. In addition, the proposed converter achieves PFC inherently across a wide load range. That provides freedom from the limited bandwidths of commercial PFC controllers and simplifies control requirements. In terms of cost, the proposed solution offers a relatively low number of components, with a single switch, two diodes (in addition to the input bridge) and two magnetic devices. The switch is referenced to ground, with a simple driving circuitry. In comparison with the work in [13], which is also designed to operate from 120 V_{rms} and delivers about the same output power, the proposed converter has a lower efficiency, yet offers a higher power factor and lower THD, with reduced component count and lower cost.

Compared with the reported resonant PFC converters, the proposed solution does not require any additional circuit or matching network, which reduces the overall system bill of materials. In addition, as the topology features an input inductor, it requires a simpler input filter and diode bridge implementations, where the input current is not pulsating as in the case of [23].

It is noted that the proposed converter's efficiency is lower than that reported by PWM converters, yet it is on par with several reported resonant converter solutions. Similar to most of the reported solutions, the proposed topology is compatible with universal input mains, as the analysis and modeling results are valid for any input voltage in the range of 85–265 V_{rms}, and inherent PFC functionality is achieved. With respect to the prototype, the switch circuit needs to be designed for the worst-case conditions, which comes with the higher input voltage. In addition, in order to ensure the validity of the FHA equations by operation near-resonance, the output voltage will change across the range of the input rms voltage. That will require the subsequent dc-dc stage to have a wide-input line regulation capability.

As the target of the presented prototype is to demonstrate the inherent PFC capability, there is a space for improvement with an optimized high-frequency design that takes benefit of the ZVS capabilities of the proposed work towards high-power-density implementations with higher efficiencies.

VI. CONCLUSION

This paper investigates the use of the class-E inverter for PFC applications. The circuit analytical model proves that the converter emulates a resistance to the input when operating with a constant duty cycle. That is asserted from the obtained state-space model, where the phase shift between the input current and voltage is shown to equal almost zero. A resonant converter incorporating a class-E inverter with a class-D rectifier is designed for the front-end ac-dc stage in a two-stage offline converter. The inherent PFC operation limits the controller responsibility to the regulation of the output voltage, which is key for resonant converters with challenging control. A prototype is built and tested to prove the concept. The prototype achieves zero-voltage switching and inherent PFC along the load range between 25 W and 211 W, with a peak efficiency of 88 %, a peak power factor of 0.99 and a minimum THD of 8.8 % at full load.

REFERENCES

- [1] B. Singh, B. N. Singh, A. Chandra, K. Al-Haddad, A. Pandey, and D. P. Kothari, "A review of single-phase improved power quality AC-DC converters," *IEEE Trans. Ind. Electron.*, vol. 50, no. 5, pp. 962–981, Oct. 2003, doi: [10.1109/TIE.2003.817609](https://doi.org/10.1109/TIE.2003.817609).
- [2] J. P. M. Figueiredo, F. L. Tofoli, and B. L. A. Silva, "A review of single-phase PFC topologies based on the boost converter," in *Proc. 9th IEEE/IAS Int. Conf. Ind. Appl. (INDUSCON)*, Sao Paulo, Brazil, Nov. 2010, pp. 1–6, doi: [10.1109/INDUSCON.2010.5740015](https://doi.org/10.1109/INDUSCON.2010.5740015).
- [3] R. T. Ryan, D. N. Hogan, R. J. Morrison, and J. G. Hayes, "Digital closed-loop control strategy to maintain the phase shift of a multi-channel BCM boost converter for PFC applications," *IEEE Trans. Power Electron.*, vol. 34, no. 7, pp. 7001–7012, Jul. 2019, doi: [10.1109/TPEL.2018.2875273](https://doi.org/10.1109/TPEL.2018.2875273).
- [4] A. Jha and B. Singh, "A bridgeless boost PFC converter fed LED driver for high power factor and low THD," in *Proc. IEEMA Eng. Infinite Conf. (eTechNXT)*, New Delhi, India, Mar. 2018, pp. 1–6, doi: [10.1109/ETECH-NXT.2018.8385333](https://doi.org/10.1109/ETECH-NXT.2018.8385333).
- [5] C. Xue, Y. Zhou, and W. Xu, "Modeling and stability analysis of parallel-connected PFC boost converter," in *Proc. Chin. Control Decis. Conf. (CCDC)*, Nanchang, China, Jun. 2019, pp. 1775–1779, doi: [10.1109/CCDC.2019.8832540](https://doi.org/10.1109/CCDC.2019.8832540).
- [6] H. Xu, D. Chen, F. Xue, and X. Li, "Optimal design method of interleaved boost PFC for improving efficiency from switching frequency, boost inductor, and output voltage," *IEEE Trans. Power Electron.*, vol. 34, no. 7, pp. 6088–6107, Jul. 2019, doi: [10.1109/TPEL.2018.2872427](https://doi.org/10.1109/TPEL.2018.2872427).
- [7] C.-Y. Yang, Y.-C. Liu, P.-J. Tseng, T.-F. Pan, H.-J. Chiu, and Y.-K. Lo, "DSP-based interleaved buck power factor corrector with adaptive slope compensation," *IEEE Trans. Ind. Electron.*, vol. 62, no. 8, pp. 4665–4677, Aug. 2015, doi: [10.1109/TIE.2015.2400421](https://doi.org/10.1109/TIE.2015.2400421).
- [8] Y.-C. Liu, F.-C. Syu, H.-C. Hsieh, K. A. Kim, and H.-J. Chiu, "Hybrid switched-inductor buck PFC converter for high-efficiency LED drivers," *IEEE Trans. Circuits Syst. II, Exp. Briefs*, vol. 65, no. 8, pp. 1069–1073, Aug. 2018, doi: [10.1109/TCSII.2017.2787554](https://doi.org/10.1109/TCSII.2017.2787554).
- [9] C. Lin, Y. Liu, H. Chiu, Y. Lo, C. Lin, P. Tseng, and S. Cheng, "Study on an interleaved buck power factor corrector with gallium nitride field effect transistor and integrated inductor," *IET Power Electron.*, vol. 7, no. 10, pp. 2506–2516, Oct. 2014, doi: [10.1049/iet-pel.2013.0642](https://doi.org/10.1049/iet-pel.2013.0642).
- [10] A. J. Hanson and D. J. Perreault, "A high frequency power factor correction converter with soft switching," in *Proc. IEEE Appl. Power Electron. Conf. Expo. (APEC)*, San Antonio, TX, USA, Mar. 2018, pp. 2027–2034, doi: [10.1109/APEC.2018.8341296](https://doi.org/10.1109/APEC.2018.8341296).
- [11] B. Zhao, A. Abramovitz, and K. Smedley, "Family of bridgeless buck-boost PFC rectifiers," *IEEE Trans. Power Electron.*, vol. 30, no. 12, pp. 6524–6527, Dec. 2015, doi: [10.1109/TPEL.2015.2445779](https://doi.org/10.1109/TPEL.2015.2445779).
- [12] M. O. Badawy, Y. Sozer, and J. A. De Abreu-Garcia, "A novel control for a cascaded buck-boost PFC converter operating in discontinuous capacitor voltage mode," *IEEE Trans. Ind. Electron.*, vol. 63, no. 7, pp. 4198–4210, Jul. 2016, doi: [10.1109/TIE.2016.2539247](https://doi.org/10.1109/TIE.2016.2539247).
- [13] A. M. Al Gabri, A. A. Fardoun, and E. H. Ismail, "Bridgeless PFC-modified SEPIC rectifier with extended gain for universal input voltage applications," *IEEE Trans. Power Electron.*, vol. 30, no. 8, pp. 4272–4282, Aug. 2015, doi: [10.1109/TPEL.2014.2351806](https://doi.org/10.1109/TPEL.2014.2351806).
- [14] A. J. Sabzali, E. H. Ismail, M. A. Al-Saffar, and A. A. Fardoun, "New bridgeless DCM Sepic and Cuk PFC rectifiers with low conduction and switching losses," *IEEE Trans. Ind. Appl.*, vol. 47, no. 2, pp. 873–881, Mar. 2011, doi: [10.1109/TIA.2010.2102996](https://doi.org/10.1109/TIA.2010.2102996).
- [15] A. Jha and B. Singh, "Cuk PFC converter for high brightness LED driver with brightness control," in *Proc. IEEE 7th Power India Int. Conf. (PIICON)*, Bikaner, India, Nov. 2016, pp. 1–6, doi: [10.1109/POWERI.2016.8077311](https://doi.org/10.1109/POWERI.2016.8077311).
- [16] C. Zhao, J. Zhang, and X. Wu, "An improved variable on-time control strategy for a CRM flyback PFC converter," *IEEE Trans. Power Electron.*, vol. 32, no. 2, pp. 915–919, Feb. 2017, doi: [10.1109/TPEL.2016.2594201](https://doi.org/10.1109/TPEL.2016.2594201).
- [17] R. W. Erickson and D. Maksimovic, *Fundamentals of Power Electronics*. Boston, MA, USA: Springer, 2007.
- [18] L. S. Mendonca, T. C. Naidon, G. G. de Freitas, M. L. D. S. Martins, and F. E. Bisogno, "Energy-based normalization for resonant power converters," *IEEE Trans. Power Electron.*, vol. 33, no. 8, pp. 6526–6536, Aug. 2018, doi: [10.1109/TPEL.2017.2784570](https://doi.org/10.1109/TPEL.2017.2784570).
- [19] M. Salem, A. Jusoh, N. R. N. Idris, H. S. Das, and I. Alhamrouni, "Resonant power converters with respect to passive storage (LC) elements and control techniques—An overview," *Renew. Sustain. Energy Rev.*, vol. 91, pp. 504–520, Aug. 2018, doi: [10.1016/j.rser.2018.04.020](https://doi.org/10.1016/j.rser.2018.04.020).
- [20] T. Nagashima, X. Wei, T. Suetsugu, M. K. Kazimierzczuk, and H. Sekiya, "Waveform equations, output power, and power conversion efficiency for class-E inverter outside nominal operation," *IEEE Trans. Ind. Electron.*, vol. 61, no. 4, pp. 1799–1810, Apr. 2014, doi: [10.1109/TIE.2013.2267693](https://doi.org/10.1109/TIE.2013.2267693).
- [21] N. J. Dahl, A. M. Ammar, and M. A. E. Andersen, "Identification of ZVS points and bounded low-loss operating regions in a class-D resonant converter," *IEEE Trans. Power Electron.*, early access, Jan. 15, 2021, doi: [10.1109/TPEL.2021.3052176](https://doi.org/10.1109/TPEL.2021.3052176).
- [22] F. M. Spliid, A. M. Ammar, and A. Knott, "Analysis and design of a resonant power converter with a wide input voltage range for AC/DC applications," *IEEE J. Emerg. Sel. Topics Power Electron.*, vol. 8, no. 3, pp. 2056–2066, Sep. 2020, doi: [10.1109/JESTPE.2019.2963266](https://doi.org/10.1109/JESTPE.2019.2963266).

- [23] A. M. Ammar, F. M. Spliid, Y. Nour, and A. Knott, "Analysis and design of a charge-pump-based resonant AC-DC converter with inherent PFC capability," *IEEE J. Emerg. Sel. Topics Power Electron.*, vol. 8, no. 3, pp. 2067–2081, Sep. 2020, doi: [10.1109/JESTPE.2020.2966143](https://doi.org/10.1109/JESTPE.2020.2966143).
- [24] A. M. Ammar, F. M. Spliid, Y. Nour, and A. Knott, "A series-resonant charge-pump-based rectifier with inherent PFC capability," in *Proc. 20th Workshop Control Modeling Power Electron. (COMPEL)*, Toronto, ON, Canada, Jun. 2019, pp. 1–5, doi: [10.1109/COMPEL.2019.8769705](https://doi.org/10.1109/COMPEL.2019.8769705).
- [25] C. Ekkaravardome, V. Chunkag, K. Jirasereeamornkul, and M. K. Kazimierczuk, "Class-D zero-current-switching rectifier as power-factor corrector for lighting applications," *IEEE Trans. Power Electron.*, vol. 29, no. 9, pp. 4938–4948, Sep. 2014, doi: [10.1109/TPEL.2013.2284872](https://doi.org/10.1109/TPEL.2013.2284872).
- [26] A. M. Ammar, Y. Nour, and A. Knott, "A high-efficiency 1 MHz 65 W GaN-based LLC resonant DC-DC converter," in *Proc. IEEE Conf. Power Electron. Renew. Energy (CPERE)*, Aswan City, Egypt, Oct. 2019, pp. 448–452, doi: [10.1109/CPERE45374.2019.8980041](https://doi.org/10.1109/CPERE45374.2019.8980041).
- [27] Y. Wang, F. Li, Y. Qiu, S. Gao, Y. Guan, and D. Xu, "A single-stage LED driver based on flyback and modified class-E resonant converters with low-voltage stress," *IEEE Trans. Ind. Electron.*, vol. 66, no. 11, pp. 8463–8473, Nov. 2019, doi: [10.1109/TIE.2018.2890502](https://doi.org/10.1109/TIE.2018.2890502).
- [28] A. M. Ammar, K. Ali, and D. J. Rogers, "A bidirectional GaN-based CLLC converter for plug-in electric vehicles on-board chargers," in *Proc. 46th Annu. Conf. IEEE Ind. Electron. Soc. (IECON)*, Singapore, Oct. 2020, pp. 1129–1135, doi: [10.1109/IECON43393.2020.9254560](https://doi.org/10.1109/IECON43393.2020.9254560).
- [29] N. J. Dahl, A. M. Ammar, A. Knott, and M. A. E. Andersen, "An improved linear model for high-frequency class-DE resonant converter using the generalized averaging modeling technique," *IEEE J. Emerg. Sel. Topics Power Electron.*, vol. 8, no. 3, pp. 2156–2166, Sep. 2020, doi: [10.1109/JESTPE.2019.2945182](https://doi.org/10.1109/JESTPE.2019.2945182).
- [30] C. Ekkaravardome, K. Jirasereeamornkul, and M. K. Kazimierczuk, "Implementation of a DC-side class-DE low-dv/dt rectifier as a PFC for electronic ballast application," *IEEE Trans. Power Electron.*, vol. 29, no. 10, pp. 5486–5497, Oct. 2014, doi: [10.1109/TPEL.2013.2290105](https://doi.org/10.1109/TPEL.2013.2290105).
- [31] J. Sasilik and J. Kamon, "The electronic ballast using class-E rectifier with tapped inductor for power factor correction," in *Proc. Int. Symp. Intell. Signal Process. Commun. Syst.*, Bangkok, Thailand, Feb. 2009, pp. 1–4, doi: [10.1109/ISPACS.2009.4806768](https://doi.org/10.1109/ISPACS.2009.4806768).
- [32] K. Jirasereeamornkul, M. K. Kazimierczuk, I. Boonyaroonate, and K. Chamngthai, "Single-stage electronic ballast with class-E rectifier as power-factor corrector," *IEEE Trans. Circuits Syst. I, Reg. Papers.*, vol. 53, no. 1, pp. 139–148, Jan. 2006, doi: [10.1109/TCSI.2005.855039](https://doi.org/10.1109/TCSI.2005.855039).
- [33] A. M. Ammar, "Advances in resonant power conversion for offline converter applications," Ph.D. dissertation, Tech. Univ. Denmark, Lyngby, Denmark, 2020.
- [34] M. Kazimierczuk and D. Czarkowski, *Resonant Power Converters*. 2nd ed. Hoboken, NJ, USA: Wiley, 2012.
- [35] M. J. Chudobiak, "The use of parasitic nonlinear capacitors in class E amplifiers," *IEEE Trans. Circuits Syst. I, Fundam. Theory Appl.*, vol. 41, no. 12, pp. 941–944, Dec. 1994, doi: [10.1109/81.340867](https://doi.org/10.1109/81.340867).
- [36] T. M. Andersen, S. K. Christensen, A. Knott, and M. A. E. Andersen, "A VHF class E DC-DC converter with self-oscillating gate driver," in *Proc. 26th Annu. IEEE Appl. Power Electron. Conf. Expo. (APEC)*, Fort Worth, TX, USA, Mar. 2011, pp. 885–891, doi: [10.1109/APEC.2011.5744699](https://doi.org/10.1109/APEC.2011.5744699).
- [37] H. Sekiya, I. Sasase, and S. Mori, "Computation of design values for class E amplifiers without using waveform equations," *IEEE Trans. Circuits Syst. I, Fundam. Theory Appl.*, vol. 49, no. 7, pp. 966–978, Jul. 2002, doi: [10.1109/TCSI.2002.800474](https://doi.org/10.1109/TCSI.2002.800474).
- [38] H. Sekiya, J. Lu, and T. Yahagi, "Design of generalized class E2 DC/DC converter," *Int. J. Circuit Theory Appl.*, vol. 31, no. 3, pp. 229–248, May 2003, doi: [10.1002/cta.229](https://doi.org/10.1002/cta.229).
- [39] P. C. Luk, S. Aldhaher, W. Fei, and J. F. Whidborne, "State-space modeling of a class E² converter for inductive links," *IEEE Trans. Power Electron.*, vol. 30, no. 6, pp. 3242–3251, Jun. 2015, doi: [10.1109/TPEL.2014.2332451](https://doi.org/10.1109/TPEL.2014.2332451).
- [40] G. Strang, *Differential Equations and Linear Algebra*. Cambridge, MA, USA: Wellesley-Cambridge, 2015, p. 510.
- [41] F. Wang and Z. Zhang, "Overview of silicon carbide technology: Device, converter, system, and application," *CPSS Trans. Power Electron. Appl.*, vol. 1, no. 1, pp. 13–32, Dec. 2016, doi: [10.24295/CPSSPEA.2016.00003](https://doi.org/10.24295/CPSSPEA.2016.00003).
- [42] J. Millán, "A review of WBG power semiconductor devices," in *Proc. Int. Semiconductor Conf. (CAS)*, Sinaia, Romania, Oct. 2012, pp. 57–66, doi: [10.1109/SMICND.2012.6400696](https://doi.org/10.1109/SMICND.2012.6400696).
- [43] J. Tsao et al., "Ultrawide-bandgap semiconductors: Research opportunities and challenges," *Adv. Electron. Mater.*, vol. 4, Jan. 2018, Art. no. 1600501, doi: [10.1002/aeml.201600501](https://doi.org/10.1002/aeml.201600501).



HUSSEIN MAHDI (Graduate Student Member, IEEE) received the B.Sc. degree in electrical power engineering from Yarmouk University, in 2011, the M.Sc. degree in environmental and renewable energy engineering from German Jordanian University (GJU), in 2015, and the second M.Sc. degree in electrical engineering from The Arctic University of Norway (UiT), in 2019, where he is currently pursuing the Ph.D. degree.

He is also working as a Graduate Research and a Teaching Assistant with The Arctic University of Norway (UiT). His research interests include resonant converters, soft switching topologies, control of power converters, and wireless power transfer.



AHMED M. AMMAR (Member, IEEE) received the B.Sc. degree in electronics and communications engineering from Mansoura University, Mansoura, Egypt, in 2011, the M.Sc. degree in microelectronics system design from Nile University, Giza, Egypt, in 2014, and the Ph.D. degree in electrical engineering from the Technical University of Denmark, Kongens Lyngby, Denmark, in 2020.

He was a Visiting Researcher with the University of Minnesota, Minneapolis, USA, and the University of Oxford, Oxford, U.K. He is currently a Postdoctoral Researcher with the Department of Electrical Engineering, Technical University of Denmark. He is also a Mentor with Siemens Business. His experience includes positions at different industries, including Intel Corporation, Hillsboro, OR, USA; Imec, Leuven, Belgium; and Mentor Graphics, Cairo, Egypt. His current research interests include power electronics, resonant power conversion, integrated power converters, power management, and delivery circuits and systems.



YASSER NOUR (Senior Member, IEEE) received the B.Sc. and M.Sc. degrees in electrical engineering from South Valley University, Aswan, Egypt, in 2007 and 2011, respectively. He received the Ph.D. degree in electrical engineering from the Technical University of Denmark, Kongens Lyngby, Denmark.

He was a Research Engineer with Enpirion Inc., a Staff Engineer with the Altera's Egypt Technology Center, and a Staff Engineer with Symmid Corporation Sdn Bhd, Malaysia. His research interests include analog integrated circuits design, integrated power converters, high-voltage low-power converters, integrated magnetics, and passive components.



MICHAEL A. E. ANDERSEN (Member, IEEE) received the M.Sc.E.E and Ph.D. degrees in power electronics from the Technical University of Denmark, Kongens Lyngby, Denmark, in 1987 and 1990, respectively.

Since 2009, he has been the Deputy Head of the Department of Electrical Engineering, Technical University of Denmark, where he is currently a Professor of power electronics. He has authored or coauthored more than 300 publications. His research interests include switch mode power supplies, piezoelectric transformers, power factor correction, and switch-mode audio power amplifiers.

...